Journal of Asian Earth Sciences 230 (2022) 105191

Contents lists available at ScienceDirect

Journal of Asian Earth Sciences

journal homepage: www.elsevier.com/locate/jseaes

# Generation of REE-rich syenite-(carbonatite) complex through lithosphere-asthenosphere interaction: An *in-situ* Sr–Nd–O isotopic study of the Mesozoic Weishan pluton, Northern China

Xi Zeng [a], Xiaochun Li [a,b,*], Hongrui Fan [a,b], Tingguang Lan [c], Jun Lan [d], Jianhui Su [e], Peng Zhang [d], Kuifeng Yang [a,b], Xinfu Zhao [e]

[a] Key Laboratory of Mineral Resources, Institute of Geology and Geophysics, Chinese Academy of Sciences, Beijing 100029, China
[b] College of Earth and Planetary Sciences, University of Chinese Academy of Sciences, Beijing 100049, China
[c] State Key Laboratory of Ore Deposit Geochemistry, Institute of Geochemistry, Chinese Academy of Sciences, Guiyang 550081, China
[d] Shandong No.5 Exploration Institute of Geology and Mineral Resources, Taian 271000, China
[e] School of Earth Resources, China University of Geosciences, Wuhan 430074, China

ARTICLE INFO

*Keywords:*
Sr-Nd-O isotopes
Asthenosphere-lithosphere interaction
Syenite-carbonatite
REE
Weishan

ABSTRACT

Carbonatite-alkaline complexes are commonly derived from the mantle. However, whether the source is lithospheric or asthenospheric mantle remains debated. In order to better understand this issue, this paper conducts a Sr-Nd-O isotopic study on the Early Cretaceous, Weishan REE-rich syenite-(carbonatite) complex, Northern China. Two types of apatite are identified from the Weishan complex, namely magmatic and xenocrystic apatite. *In-situ* Sr-Nd isotopic analyses on magmatic apatite yielded $(^{87}Sr/^{86}Sr)_i$ from 0.70690 to 0.70719, and $\varepsilon_{Nd}(t)$ from −7.6 to −8.8. The pristine calcite from carbonatite has similar $(^{87}Sr/^{86}Sr)_i$ (0.70727–0.70739) with magmatic apatite. *In-situ* oxygen isotopic analyses on zircon yielded $\delta^{18}O_{VSMOW}$(‰) from 5.9 to 6.7 ‰. Previous studies reveal that coeval, mantle lithosphere-derived rocks in the region have more enriched Sr ($^{87}Sr/^{86}Sr_i$ greater than 0.709) and Nd [$\varepsilon_{Nd}(t) \langle -12$] isotopes than the Weishan complex; whereas the asthenosphere-derived rocks in the region are characterized by depleted Sr-Nd isotopes ($^{87}Sr/^{86}Sr_i < 0.706$; $\varepsilon_{Nd}(t)$ greater than 0) and low $\delta^{18}O_{VSMOW}$ values (mostly < 5.4 ‰). It is well known that Northern China experienced destruction in the Early Mesozoic, which was accompanied with asthenosphere upwelling along *trans*-lithosphere faults. Considering that the Weishan complex locates adjacent to the *trans*-lithosphere Tanlu fault, generation of the complex may be related to asthenosphere-lithosphere interaction. Notably, the Weishan complex differs from coeval REE-barren carbonatites in that its source involved asthenosphere-derived components; hence, involvement of asthenosphere-derived components may be important for the formation of such a REE-rich complex. In general, this study highlights the importance of lithosphere-asthenosphere interaction in supplying necessary heat and materials for the generation of the Weishan complex.

## 1. Introduction

Carbonatites are specially carbon-rich magmatic rock consisting of more than 50% modal carbonate minerals (Le Maitre, 2002). In most cases, carbonatites show close temporal and spatial association with alkaline silicate rocks, such as pyroxenite, melilitite, ijolite, phonolite and syenite, forming carbonatite-alkaline complexes (Mitchell, 2005). More than 500 carbonatite-alkaline occurrences have been identified in the world, most of which are found in intracontinental rift settings or large-scale crustal lineaments (Woolley and Kjarsgaard, 2008). This type of rocks has long been of economic interest, because they are the main source of rare earth elements (REE) and niobium in the world (Verplank et al., 2016; Simandl et al., 2018). Carbonatitic-alkaline melts are commonly generated by partial melting of carbonate-rich mantle sources, as shown by experimental petrology and isotopic studies (e.g., Lee and Wyllie, 1998; Yaxley and Brey, 2003; Bell and Simonetti, 2010; Jones et al., 2013; Chen and Simonetti, 2015; Yaxley et al., 2022). Owing to their mantle origins, carbonatite-alkaline complexes are excellent recorders of mantle processes and the tectonic processes that allow their emplacement in the crust (Woolley and Bailey, 2012).

* Corresponding author at: Key Laboratory of Mineral Resources, Institute of Geology and Geophysics, Chinese Academy of Sciences, Beijing 100029, China (X. Li).
*E-mail address:* lixiaochun86@gmail.com (X. Li).

https://doi.org/10.1016/j.jseaes.2022.105191
Received 19 December 2021; Received in revised form 14 March 2022; Accepted 16 March 2022
Available online 21 March 2022

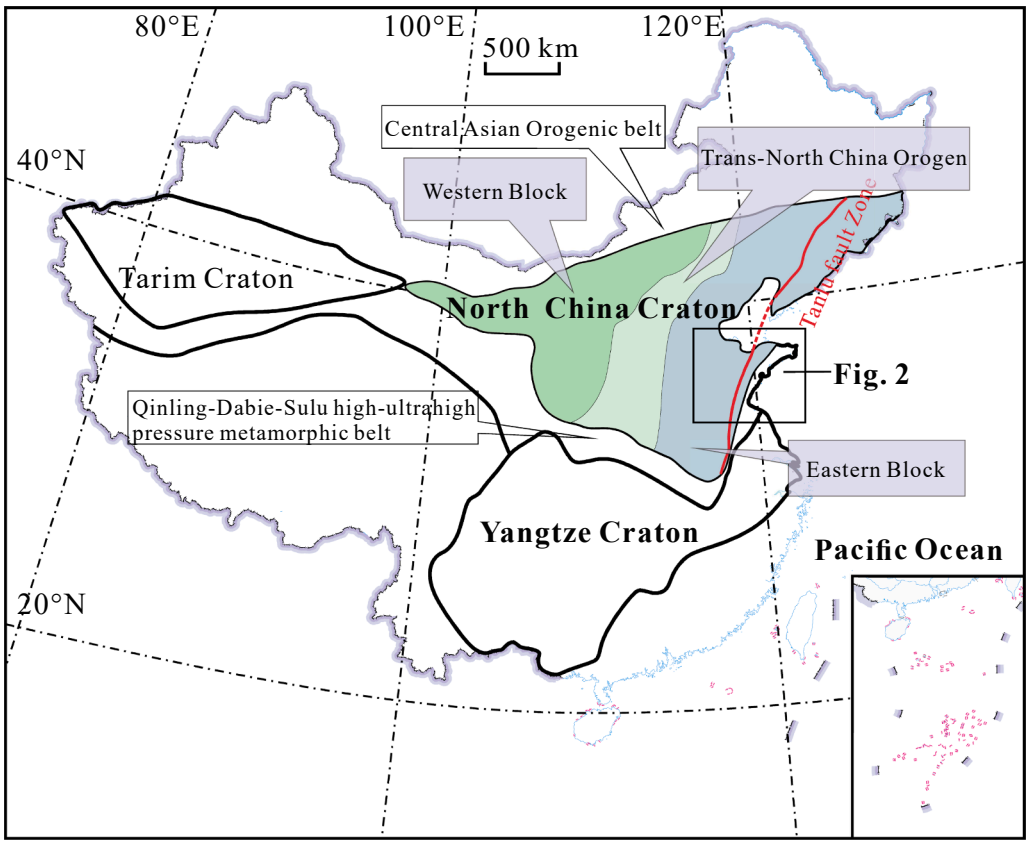


**Fig. 1.** (a) Simplified tectonic map showing major tectonic units of North China. The location of the North China Craton is highlighted (modified after Zhao et al., 2001).

Although carbonatites are well known to be mantle origin, whether the magma source is lithospheric or sub-lithospheric (asthenospheric) mantle remains an unresolved issue (Bell, 2020). On the one hand, the vast majority of carbonatite-alkaline complexes are found on continents, with only few in oceanic areas (The Canary, Cape Verde and Kerguelen Islands; Hoernleet al., 2002). In addition, carbonatites and alkaline rocks are deposited repeatedly at intervals of hundreds of millions of years in some areas. According to these observations, it is proposed that the carbonatite-alkaline complexes are mainly sourced from a sub-continental lithospheric mantle source (Woolley and Bailey, 2012). Typical examples that are thought to be sourced from sub-continental lithospheric mantle include the Eppawala carbonatites, Sri Lanka (Manthilake et al., 2008), the Nam Xe carbonatite, Vietnam (Thi et al., 2014), and the Maoniuping carbonatite complex, China (Hou et al., 2015). On the other hand, a few carbonatite-alkaline complexes show close petrogenetic and temporal association with large igneous provinces, such as the Oka carbonatite in Canada (Chen and Simonetti, 2015), the Amba Dongar carbonatite in India (Simonetti et al., 1998), the Kola Peninsula carbonatites in Russia (Zaitsev et al., 2014), and the Tarim carbonatite in northwestern China (Cheng et al., 2017). It is also notable that many carbonatites show primitive noble gas isotopic signatures, and their radiogenic isotope ratios are similar as oceanic island basalts (OIB) (i.e., involving HIMU, EM1 and FOZO mantle components) (Bell and Simonetti, 2010). It's difficult to reconcile such observations with a lithospheric origin. As a result, some researchers believe that the carbonatites are derived from the asthenospheric mantle/mantle plume, with the overlaying lithosphere playing a key role in their preservation.

In order to better understand the mantle source(s) of carbonatite-alkaline complexes, more studies on natural examples are required. Radiogenic isotopic tracing can effectively discriminate lithospheric mantle from asthenospheric mantle, as these two mantle reservoirs commonly have different isotope signatures in a region (Bell and Simonetti, 2010; Woolley and Bailey, 2012; Hofmann, 2014). Oxygen isotopes also have the potential to distinguish lithospheric mantle from asthenospheric mantle, provided that the two mantle reservoirs were metasomatized by different agents (Deines et al., 1989; Eiler et al., 1997; Liu et al., 2014; Zhu et al., 2017). Therefore, a Sr, Nd, and O isotopic study of natural carbonatite-alkaline complexes may help unravel the source(s) of this type of rocks.

The Weishan REE-rich syenite-(carbonatite) complex in the eastern North China Craton (NCC), China is a well-suited example for such study. This complex was generated under the background of destruction of NCC (Lan et al., 2011; Wang et al., 2019). It is notable that a series of broadly coeval rocks derived from lithosphere and asthenosphere, respectively, have been identified adjacent to the Weishan complex. A comparative study of the Weishan complex with these mantle-derived rocks has a great potential to elucidate the magma source and deep process that led to the formation of this REE-rich complex.

In this study, we conduct a Sr, Nd and O isotopic study on the Weishan syenite-(carbonatite) complex. Considering that whole-rock isotopic analyses may yield mixed or misleading rock-forming information, micro-scale isotopic analyses were conducted on minerals to obtain the isotopic signatures of primary magmas. Specifically, in-situ Sr isotopic composition of apatite and calcite, and Nd isotopic composition of apatite were obtained using laser ablation multi-collector inductively coupled plasma mass spectrometry (LA-MC-ICP-MS), and in-situ O isotopic composition of zircon was obtained using secondary ion mass spectrometry (SIMS). The dataset indicates that both lithospheric and asthenospheric mantle reservoirs have contributed to the formation of the Weishan complex. A comparison of the REE-rich Weishan carbonatite with REE-barren carbonatite in the region further implies that involvement of asthenosphere-derived components may be important for the enrichment in REE in the Weishan complex.

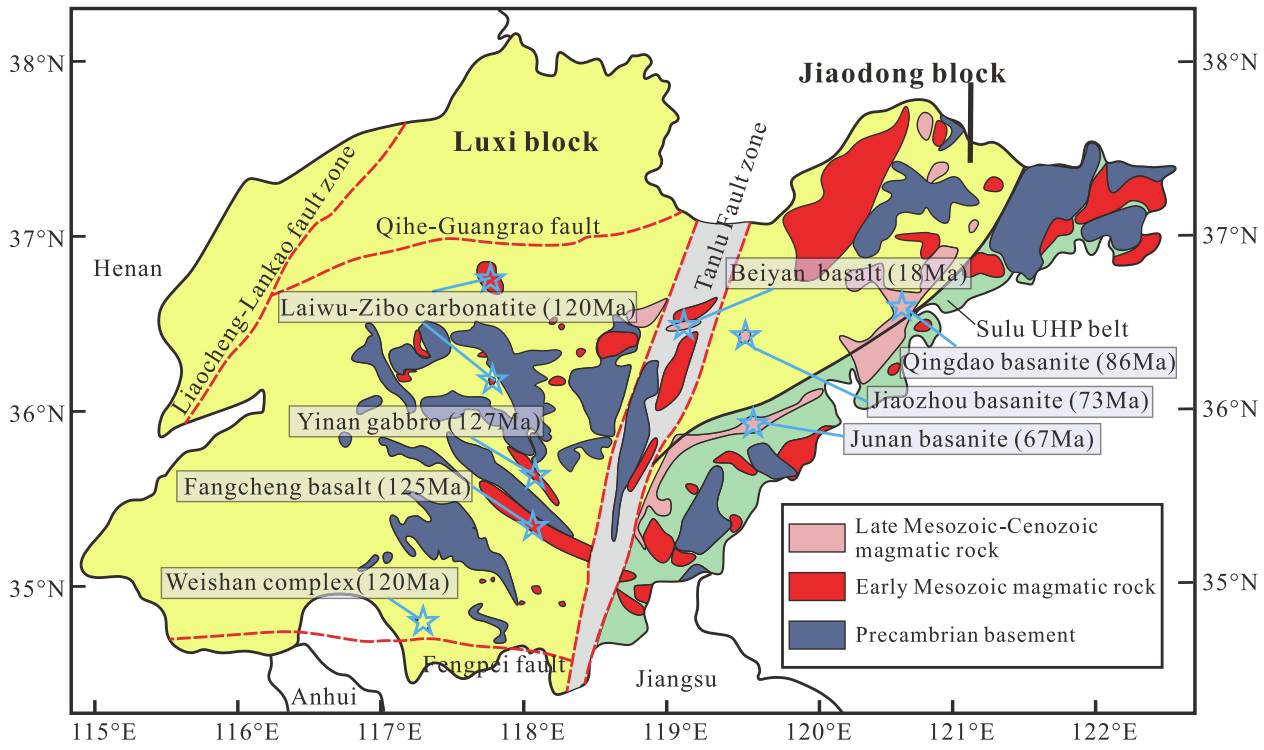


**Fig. 2.** Simplified geological map of the Shandong province in the eastern North China Craton, showing the distribution of Mesozoic and Cenozoic magmatic rocks (modified after Zhang et al. 2002). Note that some representative Early Mesozoic-Cenozoic mantle-derived rocks are highlighted by starts.

## 2. Regional Geology

### 2.1. The North China Craton

The North China Craton (NCC), bordered by the Central Asian Orogenic belt to the north and the Qinling-Dabie-Sulu high-ultrahigh pressure metamorphic belt to the south, is the oldest and largest craton in China. It can be tectonically separated into three parts: the Eastern Block, the Western Block, and the Trans-North China Orogen (Zhao et al., 1998; Fig. 1). Following cratonization at ~ 2.5 Ga, the Eastern and Western Blocks were amalgamated together along the Trans-North China Orogen at ~ 1.88 Ga (Zhao et al., 2001). Since that event, the NCC has been generally stable from the Late Paleoproterozoic until the Mesozoic.

Multiple subduction and collisional events occurred from Paleozoic to Mesozoic surrounding the NCC, including the southward subduction of the Paleo-Asian Ocean below the northern margin of the NCC during the Ordovician and Permo-Triassic (Xiao et al., 2003), the northward continental collision between the Yangtze Plate and the southern NCC during the Triassic (Li et al., 1993; Meng and Zhang, 1999), and westward subduction of the Paleo-Pacific Plate underneath the eastern Asian continent during the Mesozoic (Xu et al., 2013). In response to these subduction and collisional events, the eastern part of the NCC became tectonically active since the Mesozoic, during which the cold, thick, and refractory cratonic lithosphere (~200 km) in the Paleozoic was replaced by a hot, thin (<80 km), and fertilized one (Menzies et al., 1993; Griffin et al., 1998). This transition was accompanied with widespread magmatism (Yang et al., 2021), gold mineralization (Fan et al., 2005; Zhu et al., 2015), formation of metamorphic core complexes and half-graben basins (Davis et al., 2001; Zhu et al., 2021), and activation of large-scale strike-slip fault (the Tan-Lu fault) (Zhu et al., 2016; 2018). These geological observations indicate that the NCC became unstable and experienced destruction in the Mesozoic (Zhu et al., 2012).

### 2.2. The Luxi terrane

The Shandong province occupies the eastern edge of the Eastern Block of the NCC and is geologically subdivided into the Luxi and Jiaodong terranes (Fig. 2), which is separated by the Tanlu fault zone. The Luxi Terrane is bounded by the Tanlu fault zone to the east, the Liaocheng-Lankao fault zone to the west, the Qihe-Guangrao fault to the north, and the Fengpei fault to the south (Fig. 2). Lithologically, the Luxi Terrane comprises Precambrian basement rocks (including Neoarchean TTG gneisses and amphibolites, and Paleoproterozoic granitoids), Paleozoic kimberlite and carbonates interbedded with clastic rocks, and Mesozoic continental clastic and volcaniclastic rocks (Lan et al., 2011; Wang et al., 2008). These rocks are intruded by a series of Mesozoic plutons that were generated during the destruction of NCC.

At the main stage of the destruction of NCC, widespread magmatic rocks were generated in the Luxi terrane, including those in the Early Jurassic and Early Cretaceous. The Early Jurassic magmatic rock is represented by Tongshi syenitic pluton (180 Ma, Lan et al., 2012). The Early Cretaceous magmatic rocks are mainly composed of mantle-derived gabbros (Yinan gabbro, 127 Ma; Xu et al., 2004), basalts (Fangcheng basalt, 124 Ma; Zhang et al., 2002) and carbonatite-syenite complexes (Laiwu-Zibo carbonatite, 123–113 Ma, Ying et al., 2004; Weishan pluton), and the crust-derived high-Mg diorites (~130 Ma, Duan et al., 2017) and granites (133–128 Ma, Hu et al., 2010). The development of these magmatic rocks is closely related to the Tanlu Fault, which is considered to be transverse from the crust to the crust-mantle boundary.

After the climax of the destruction of NCC, magmatic rocks are rare. To our knowledge, Late Cretaceous magmatic rocks have not been identified in the Luxi terrane. However, a few Late Cretaceous to Cenozoic mafic rocks are developed in the Tanlu fault zone and the Jiaodong terrane (Fig. 2), such as the Junan, Jiaozhou and Qingdao basanites (86–66 Ma, Dai et al., 2019a,b), and the Beiyan basalt (18 Ma, Xiao et al., 2010).

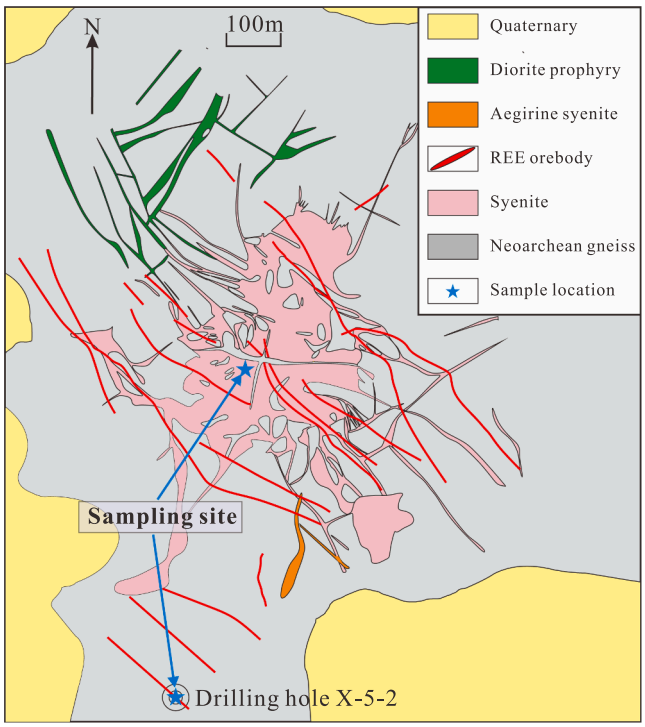


**Fig. 3.** Detailed geological map of the Weishan complex (modified after Zhou et al., 2013).

### 2.3. The Weishan syenite-(carbonatite) complex and associated REE ore

The Weishan syenite-(carbonatite) complex is located on the southwestern margin of Luxi block, close to the Fengpei fault (Fig. 2). The complex covers an area of ~4 $km^2$, and extends from northwest to southeast as dendroid intruding into Late Archean gneissic granodiorite. The Weishan complex is dominated by syenite, with subordinate aegirine syenite and carbonatite (Figs. 3 and 4). A series of dioritic dikes have developed adjacent to, but without genetic association with, the Weishan complex. In the Weishan complex, syenite is mainly composed of K-feldspar (50 vol%), albite (35 vol%), perthite (10 vol%), and quartz (4 vol%). The accessory minerals include biotite, zircon, apatite and thorianite (Fig. 4a and 5a). Aegirine syenite occurs as small stocks in the outer part of the complex. It mainly consists of K-feldspar (50 vol%), albite (35 vol%), perthite (5 vol%), quartz (5 vol%), and aegirine (2 vol %) (Fig. 4b and 5b), with rare apatite and zircon. Some syenite and aegirine syenite samples have been variably overprinted by carbonatitic fluids, so they may contain certain amounts of calcite (Fig. 4c and 5c). They may also contain small amounts of later-stage hydrothermal minerals (e.g., celestite, barite, fluorite, chlorite, and sulfides) (Fig. 5a to 5c). Previous studies (Lan, 2011) show that the bulk-rock syenites have high contents of $SiO_2$ (63.4–70.1 wt%), $Al_2O_3$ (13.4–15.8 wt%), $Na_2O + K_2O$ (9.6–10.6 wt%), and low contents of FeO (0.60–1.65 wt%) and MgO (0.17–0.49 wt%), reflecting the dominance of feldspars in the rocks. Their CaO contents are variable (0.3–5.6 wt%), which is related to the presence of variable amounts of calcite in the samples. The syenite samples have high contents of REE (1104–2128 ppm), Sr (409–3053 ppm) and Ba (2627–9507 ppm), and are depleted in high-field strength elements (HFSE: Nb, Ta, Zr, Hf, and Ti). In the chondrite-normalized REE diagram, the syenite samples are characterized by highly LREE-enriched patterns, with $(La/Yb)_N$ ratios of 113 to 276.

The carbonatites are mainly composed of coarse-grained calcite (Fig. 5d). The calcite grains may have been variably overprinted by bastnaesite, celestite, barite, fluorite, and parasite. In the contact of syenite and carbonatite, calcite grains occur overprinting feldspar grains (Fig. 4c and 5c). Such observations indicate that carbonatite represents a late-crystallizing carbonthermal phase from the $CO_2$-rich silicate magma. The Weishan complex has been dated using zircon U-Pb and muscovite Rb-Sr geochronometers, yielding an age of ~ 120 Ma (Lan et al., 2011).

Notably, the Weishan syenite-(carbonatite) complex is accompanied with REE mineralization (Fig. 4e and 4f), forming the third largest REE deposit in China with a total reserve of 0.19 Mt rare earth oxides (REO) with an average grade of 4.61 wt% (Jia and Liu, 2020). Recent-year drilling program has outlined an additional ~ 1 Mt REO. In this deposit, bastnäsite ($REECO_3F$) is the major REE ore mineral, and there is also subordinate parisite [$CaREE(CO_3)_2F$]. Bastnäsite and parasite commonly occur in association with Sr-Ba sulfate (barite and celestite), fluorite, and calcite (Fig. 5e and 5f). In the outer part of the complex, the REE minerals and associated gangue minerals commonly occur as veinlets or disseminations overprinting the ore-related pluton; whereas toward the inner and upper parts of the complex, the REE and hydrothermal minerals commonly form wider veins of 0.1–1 m cutting through the pluton.

## 3. Sample description

Apatite grains from four syenite samples were selected for study: two are fresh syenite (21WSK04 and 21WSK10) and the other two (21WS07 and 21WS08) are carbonate-bearing syenite (Table 1). Petrographic observations show that two types of apatite occur in syenite. Type-1 apatite grains occur in samples 21WSK04, 21WSK10, and 21WS07. They are euhedral to subhedral in shape, with sizes of 20 to 100 μm, and show co-existed relationship with feldspar (Fig. 6a to 6c). Under BSE imaging, they show well-defined grow zonation (Fig. 6a to 6c). In contrast, type-2 apatite grains (in sample 21WS08) are anhedral in shape, and have smaller sizes than type-1 grains. Under BSE images, they do not display visible zonation (Fig. 6d and 6e).

Calcite grains from two syenite (21WS06 and 21WS09) and two carbonatite (21WS01 and 21WS02) samples were chosen for study (Table 1). In the syenites, calcite mainly occurs as anhedral grains (20–200 μm) overprinting feldspar or quartz (Fig. 5c); whereas calcite from the carbonatite mainly occurs as larger (100–500 μm), euhedral grains (Fig. 5d).

Zircon grains were separated from a carbonate-bearing syenite sample (21WS03) for study (Table 1). The zircon grains are pale brown to colorless, and show prismatic or di-pyramidal morphology. Crystal lengths range from 50 to 100 μm, with length/width ratios ranging from 1:1 to 1.5:1. In CL images, the zircon grains show sector or faint oscillatory zoning (Fig. 6f).

## 4. Analytical methods

### 4.1. In-situ trace element analysis

The trace elements of apatite and calcite were analyzed by an Agilent 7700x ICP-MS, coupled with an Analyte Excite193 nm excimer laser ablation system at Nanjing FocuMS Analysis Lab, China. The deep ultraviolet beam generated by the excimer laser generator was focused on the surface of the mineral through the homogenization light path, and the laser energy density was 3.2 $J/cm^2$. The beam spot diameter was 40 μm, the frequency was 7 Hz. The denudation aerosol was sent by helium into the ICP-MS for testing. Each analysis consisted of approximately 30 s of background value collection and 40 s of sample data collection. NIST 610 glass was used as an external calibration standard, and CaO as an internal standard. The original test data was processed offline by the ICPMSDataCal10.2 software. The trace element data are listed in Supplementary Table 1.

### 4.2. In-situ Sr isotopic analysis

The in-situ Sr isotope ratios of apatite and calcite were analyzed

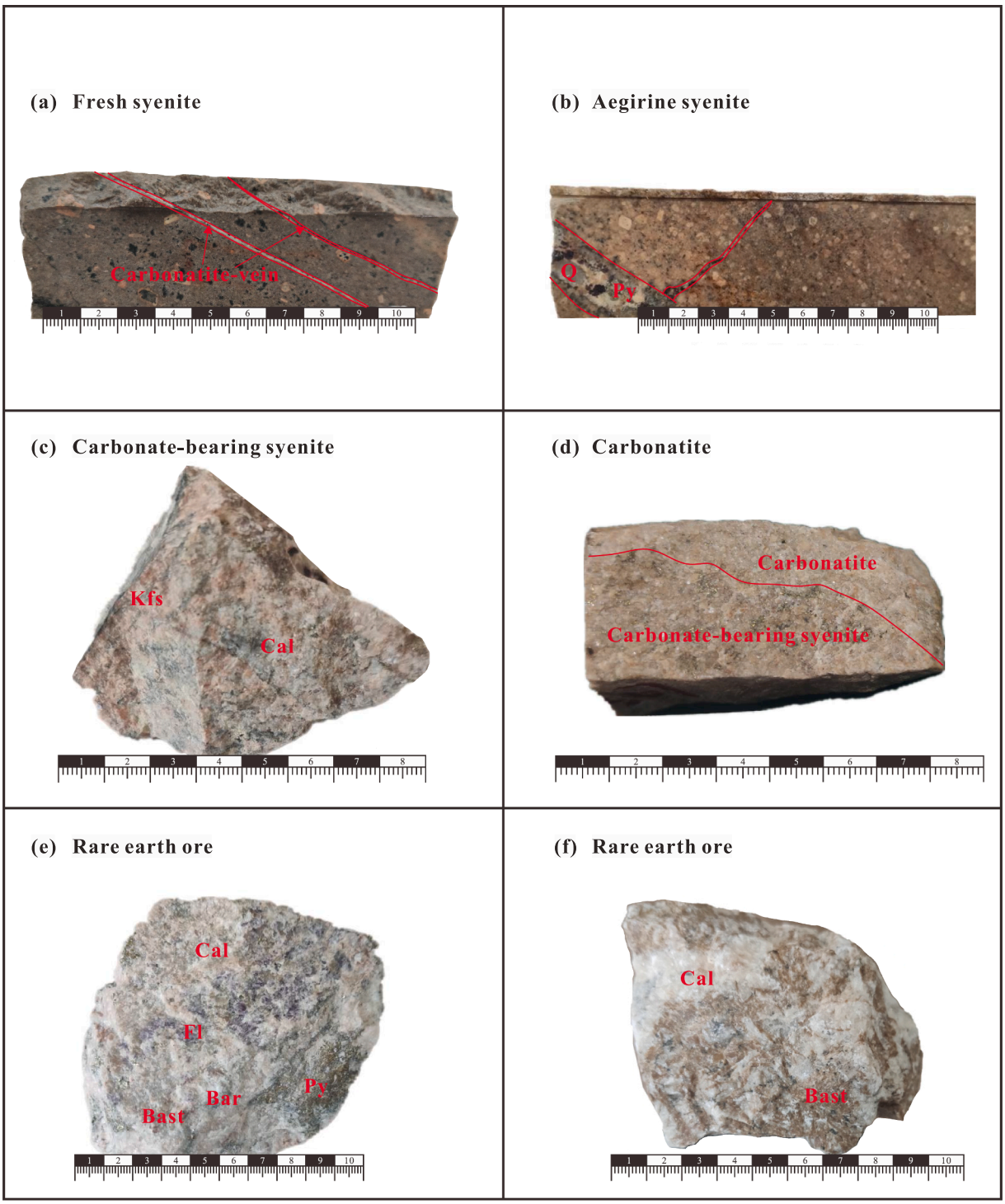


**Fig. 4.** Hand specimen of rock and ore samples from the Weishan complex. (a) A fresh syenite sample cut by some thin carbonatite veins. (b) An aegirine syenite sample which is overprinted by later-stage hydrothermal minerals. (c) A syenite sample overprinted by disseminated calcite. (d) A sample containing both syenite and carbonatite. (e) A rare earth ore sample containing several hydrothermal minerals (e.g., calcite, fluorite, bastnaesite and pyrite). (f) A rare earth ore sample containing abundant large bastnaesite grains. Mineral abbreviations: Bar-barite, Bast-bastnaesite, Cal-calcite, Fl-fluorite, Kfs-K-feldspar, Py-pyrite, Q-quartz.

using a Neptune Plus MC-ICP-MS in combination with a Geolas HD excimer ArF laser ablation system at the Wuhan Sample Solution Analytical Technology Co., Ltd, China. The spot width for a single laser spot ablation varied from 60 to 160 μm, depending on the Sr signal intensity. The laser energy density was kept constant at 10 J/cm$^2$ despite the pulse frequency ranging from 8 to 15 Hz. Helium was employed as the carrier gas for the ablation cell in the laser ablation system. Nine Faraday cups with 1011 Ω resistors were installed on the Neptune Plus. The mass system's Faraday collector setup consisted of an array from L4 to H3 that monitored Kr, Rb, Er, Yb, and Sr. Potential isobaric interference corrections were made. Firstly, the regions of integration for both gas background and sample were selected. Following background correction, which removes the background $Kr^+$ signals, no additional Kr peak stripping was applied. Interferences of $^{168}Er^{++}$on$^{84}Sr$, $^{170}Er^{++}$and$^{170}Yb^{++}$on$^{85}Rb$, $^{172}Yb^{++}$on$^{86}Sr$, and $^{174}Yb^{++}$on$^{87}Sr$ were corrected based on the measured signal intensities of $^{167}Er^{++}$, $^{173}Yb^{++}$as

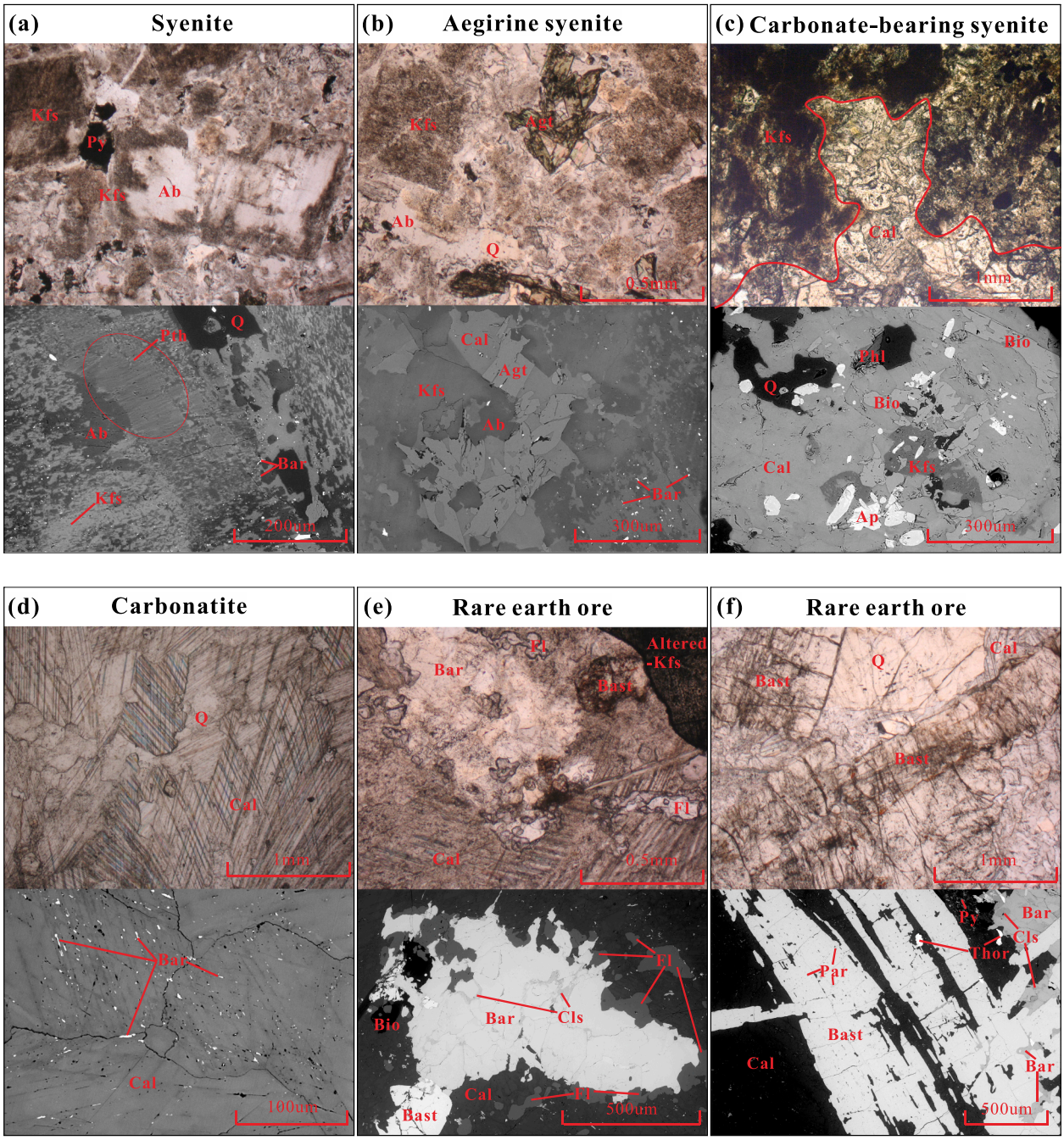


**Fig. 5.** Transmitted light microphotographs and back scattered electron (BSE) images of rock and ore samples from the Weishan complex. (a) Syenite mainly containing K-feldspar, albite, quartz and perthite. Sparse later-stage barite and pyrite can also be identified. (b) Aegirine syenite mainly consisting of aegirine, K-feldspar, albite and quartz. (c) Carbonatite dominated by large calcite grains. (d) Syenite overprinted by carbonatite. (e) An ore sample mainly containing barite, celestite, fluorite and bastnaesite. (f) High-grade ore sample containing abundant bastnaesite crystals. Mineral abbreviations: Ab-albite, Agt-aegirine, Bar-barite, Bast-bastnaesite, Bio-biotite, Cal-calcite, Chl-chlorite, Cls-celestite, Fl-fluorite, Kfs-K-feldspar, Par-parisite, Phl-phlogopite, Pth-perthite, Py-pyrite, Q-quartz, Thor-thorianite.

well as the natural isotope ratios of Er and Yb. The isobaric interference of $^{87}$Rb on$^{87}$Sr was corrected by monitoring the$^{85}$Rb, and the natural ratio of $^{85}$Rb/$^{87}$Rb = 2.5926 was used for correction of isobaric Rb interference by the exponential law, assuming that Rb has the same mass discrimination as Sr. Following the interference corrections, the mass fractionation of Sr isotopes was corrected using the exponential law, assuming $^{88}$Sr/$^{86}$Sr = 8.375209. All data reduction for the MC-ICP-MS analysis of Sr isotope ratios was conducted using "Iso-Compass" software. Two natural apatites, Durango and MAD, were used as the unknown samples to monitor the accuracy of the analytical procedure. The in-situ Sr isotopic data of samples and monitor standards are listed in Supplementary Table 2.

### 4.3. *In-situ Sm-Nd isotopic analysis*

In-situ Sm-Nd isotope analysis of apatite was conducted by a Neptune Plus MC-ICP-MS equipped with a Geolas HD excimer ArF laser ablation system at the Wuhan Sample Solution Analytical Technology Co., Ltd, China. During the analysis, helium was employed as the carrier gas in the laser ablation system, and it was then combined with argon

**Table 1**
A list of samples used in this study.

| Mineral | | Sample | Sampling site | Rock type | Rock feature |
|---|---|---|---|---|---|
| Apatite | Type-1 Ap | 21WSK04 | Drilling borehole at the depth of 512 m | Fresh syenite | Porphyritic texture with K-feldspar and albite phenocrysts (20–30%) and matrix consists of K-feldspar (35%-40%), albite (30–35%) and quartz (10%) |
| | | 21WSK10 | Drilling borehole at the depth of 702 m | Fresh syenite | |
| | | 21WS07 | Outcrops in the center of the Weishan complex | Carbonate-bearing syenite | Syenite with K-feldspar (40%), albite (40%) and quartz (15%) overprinted by carbonatite and later-stage hydrothermal minerals |
| | Type-2 Ap | 21WS08 | | Carbonate-bearing syenite | |
| Zircon | | 21WS03 | | Carbonate-bearing syenite | |
| Calcite | | 21WS06 | | Carbonate-bearing syenite | |
| | | 21WS09 | | Carbonate-bearing syenite | |
| | | 21WS01 | | Carbonatite | Medium- to coarse-grained texture with calcite (70%-90%) and later-stage hydrothermal minerals (10%-30%) |
| | | 21WS02 | | Carbonatite | |

following the ablation cell. To improve the analytical sensitivity, small amounts of nitrogen were added to the argon makeup gas flow. The spot diameter ranged from 32 to 90 μm dependent on Nd contents in the samples. The pulse frequency ranged from 4 to 10 Hz. The laser energy density was set at ~ 8 J/cm$^2$. The Neptune Plus was equipped with nine Faraday cups fitted with 1011 Ω resistors. In Faraday cups, the isotopes $^{142}$Nd,$^{143}$Nd,$^{144}$Nd,$^{145}$Nd,$^{146}$Nd,$^{147}$Sm,$^{148}$Nd and$^{149}$Sm were collected in static mode. The mass discrimination factor for$^{143}$Nd/$^{144}$Nd was determined using$^{146}$Nd/$^{144}$Nd with the exponential law. Using the$^{144}$Sm/$^{149}$Sm ratio of 0.2301, the$^{149}$Sm signal was utilized to rectify the residual on$^{144}$Nd. The mass fractionation of $^{147}$Sm/$^{149}$Sm was adjusted using the $^{147}$Sm/$^{149}$Sm ratio of 1.08680 and exponential law. Data reduction was conducted using "Iso-Compass" software. Two natural apatite megacrysts, Durango and MAD, were utilized as unknown samples to monitor the accuracy of the analytical procedure. The in-situ Sm-Nd isotopic data of samples and monitor standards are listed in Supplementary Table 3.

### 4.4. *In-situ zircon O isotope analyses*

In-situ zircon O isotope analyses were conducted at the Institute of Geology and Geophysics (IGG), Chinese Academy of Sciences (CAS) in Beijing, using a CEMECA IMS 1280-HR. The $Cs^+$ primary ion beam was used as the ion source. Spot size of about 20 μm was applied. Oxygen isotopes were measured using multi-collection mode on two off-axis Faraday cups. Measured $^{18}O/^{16}O$ ratios were standardized to V-SMOW compositions ($^{18}O/^{16}O$ = 0.0020052), and then corrected for the instrumental mass fractionation factor (IMF). The IMF was obtained using the zircon standard 91,500 with a $\delta^{18}O$ value of 9.9 ‰ (Wiedenbeck et al., 2004). Uncertainties on individual analysis are usually better than 0.2–0.3 ‰. A second zircon standard, Qinghu, was measured to monitor the accuracy of the analytical procedure. Nine measurements of the Qinghu zircon standard yielded a weighted mean $\delta^{18}O$ value of 5.53 ± 0.1 ‰(2σ), which is consistent, within uncertainties, with the reported value of 5.4 ± 0.2 ‰(2σ) (Li et al., 2013). The zircon oxygen isotope data are listed in Supplementary Table 4.

## 5. Analytical results

### 5.1. *In-situ trace element compositions of apatite and calcite*

Type-1 apatite has high REE contents (12002–65029 ppm, 28213 ppm on average). In the chondrite-normalized REE diagrams, they are characterized by steeply right-inclined patterns (Fig. 7a), with $(La/Yb)_N$ values ranging from 101 to 409 (232 on average). In addition to REE, type-1 apatite also has high contents of Sr, Th, U, Ge, Ga and V

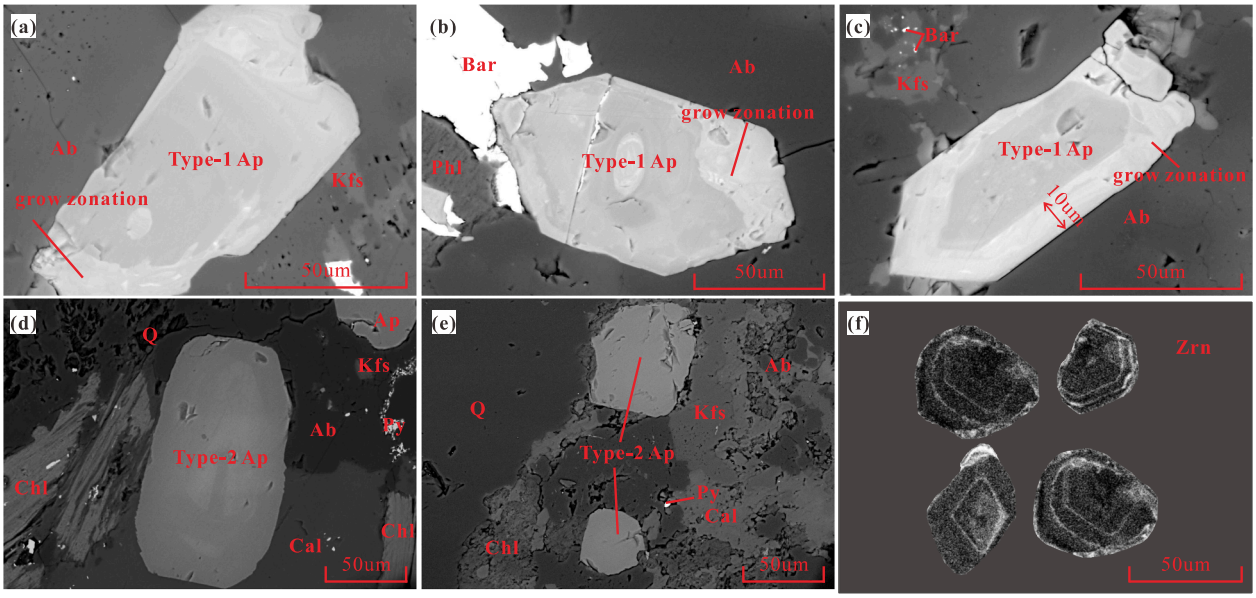


**Fig. 6.** (a)~(c) BSE images of type-1 apatite. (d)~(e) BSE images of type-2 apatite. (f) CL image of zircon grains. Mineral abbreviations: Ab-albite, Ap-apatite, Bar-barite, Cal- calcite, Chl-chlorite, Kfs-K-feldspar, Phl-phlogopite, Py-pyrite, Q-quartz, Zrn-zircon.

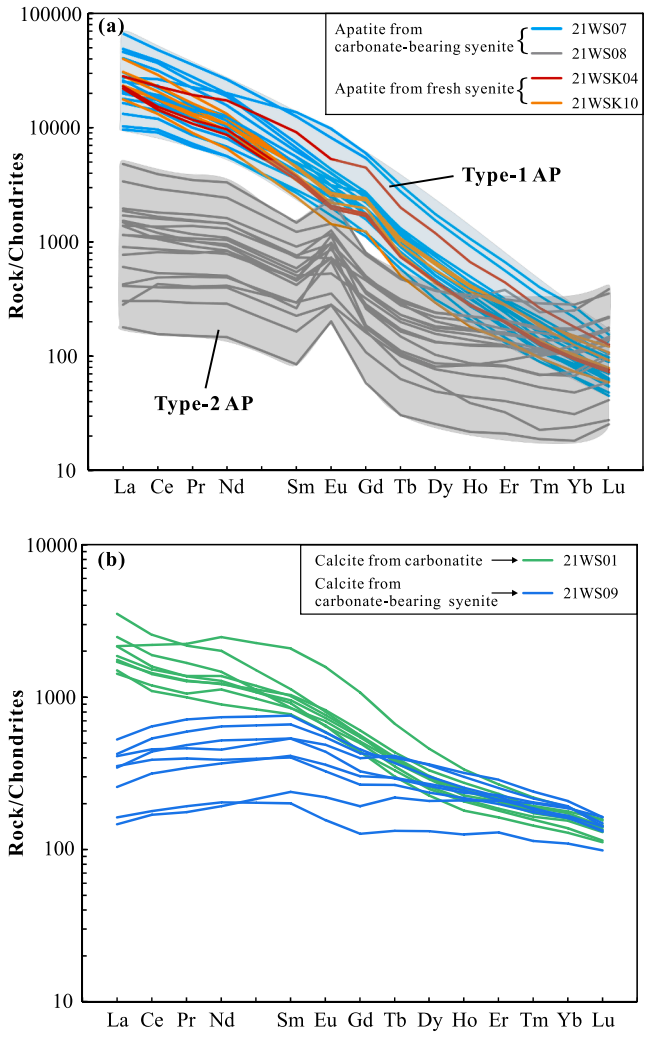


**Fig. 7.** (a) Chondrite-normalized REE patterns for apatite in syenite from the Weishan complexes. (b) Chondrite-normalized REE patterns for calcite from the Weishan complexes.

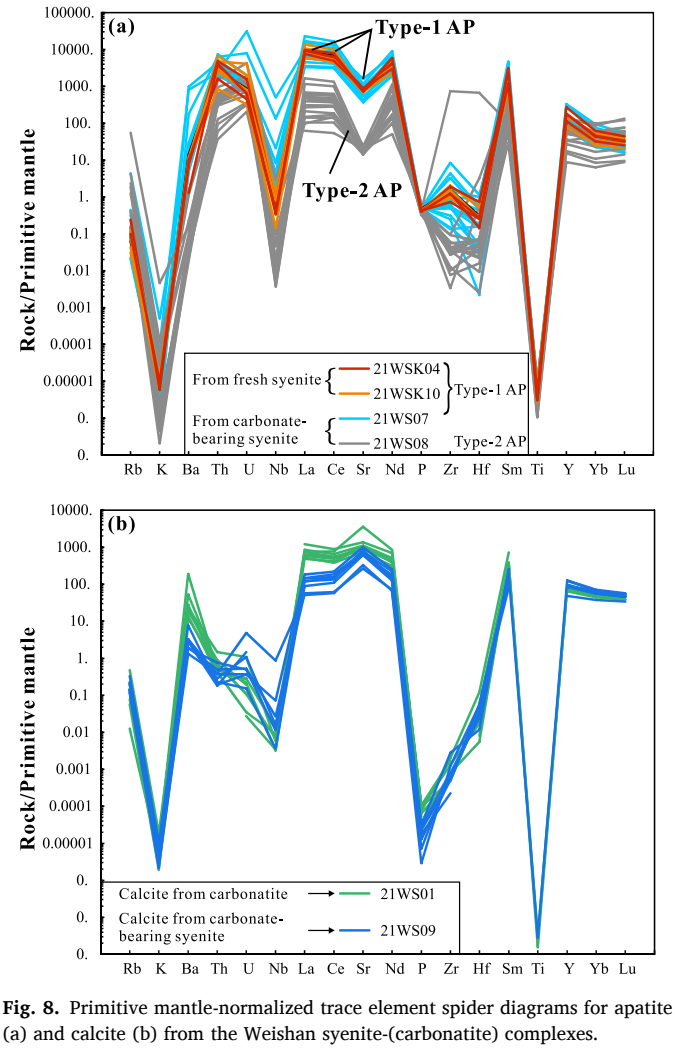


**Fig. 8.** Primitive mantle-normalized trace element spider diagrams for apatite (a) and calcite (b) from the Weishan syenite-(carbonatite) complexes.

(Appendix Table 1). The contents of high-field strength elements (e.g., Nb, Ti, Zr and Hf) are substantially low (Appendix Table 1; Fig. 8a).

Type-2 apatite has much lower REE contents (276 to 6210 ppm, 1989 ppm on average) than type-1 apatite. The fractionation between light and heavy rare earths is less obvious than type-1 apatite (Fig. 7a), with $(La/Yb)_N$ values ranging from 3.4 to 19.0 (10.7 on average). Type-2 apatite also contains moderate to high Ba, Th, and U, but their contents are generally lower than those in type-1 apatite (Fig. 8a).

Calcite grains from a carbonatite (21WS01) and a syenite (21WS09) sample were analyzed. Those from carbonatite has high REE contents (1930–4105 ppm, 2827 ppm on average), whereas those from syenite has obviously lower REE contents (417 to 1351 ppm, 884 ppm on average). In the chondrite-normalized REE diagrams, calcite from both samples show right-inclined patterns (Fig. 7b), with those from sample 21WS01 displaying more obvious LREE-HREE fractionation. In addition to REE, the calcite grains also contain 20590 ppm Sr, 165 ppm Ba, 29 ppm Pb on average. The contents of Nb, P, Zr, Hf, and Ti are substantially low (Fig. 8b).

### 5.2. *In-situ Sr isotopic compositions of apatite and calcite*

Both apatite and calcite have substantially low $^{87}Rb/^{86}Sr$ ratios (<0.01). Type-1 apatite grains from relatively fresh syenite (21WSK04 and 21WSK10) have $^{87}Sr/^{86}Sr$ ratios ranging from 0.70690 to 0.70719, while those from syenite overprinted by hydrothermal minerals (21WS07) have slightly higher $^{87}Sr/^{86}Sr$ ratios (0.70745 to 0.70789) (Fig. 9a). Compared with type-1 apatite, type-2 apatite grains (21WS08) have an obviously wider range of $^{87}Sr/^{86}Sr$ ratios (0.70391 to 0.71686) (Fig. 9b).

Calcite grains from the carbonatite samples and syenite samples have slightly higher $^{87}Sr/^{86}Sr$ ratios than apatite from fresh syenite, while their $^{87}Sr/^{86}Sr$ ratios are similar with apatite from carbonate-bearing syenite (Fig. 9a). Specifically, calcite grains from carbonatite (21WS01, 21WS02) have $^{87}Sr/^{86}Sr$ ratios ranging from 0.70753 to 0.70780, and those from syenite overprinted by hydrothermal minerals (21WS06) have slightly lower $^{87}Sr/^{86}Sr$ ratios (0.70727 to 0.70739).

### 5.3. *In-situ Sm-Nd isotopic compositions of apatite*

Type-1 apatite grains from fresh syenite (21WSK04, 21WSK10) have $^{147}Sm/^{144}Nd$ from 0.071357 to 0.136619, and $^{143}Nd/^{144}Nd$ from 0.512101 to 0.512167. When corrected to 120 Ma, the $\varepsilon_{Nd}(t)$ values range from −8.8 to −7.6. Type-1 grains from syenite overprinted by hydrothermal minerals (21WS07) have $^{147}Sm/^{144}Nd$ from 0.074046 to 0.103800, and $^{143}Nd/^{144}Nd$ from 0.512032 to 0.512066. Their $\varepsilon_{Nd}(t)$ values are slight lower (-10.2 to −9.3) than those from fresh syenite (Fig. 9c).

Type-2 apatite grains from the carbonate-bearing syenite (21WSK08) have $^{147}Sm/^{144}Nd$ from 0.083722 to 0.146288, and $^{143}Nd/^{144}Nd$ from 0.510875 to 0.511988. When corrected to 120 Ma, they have highly varied $\varepsilon_{Nd}(t)$ values (-28.3 to −11.9) (Fig. 9d). It is noteworthy that the

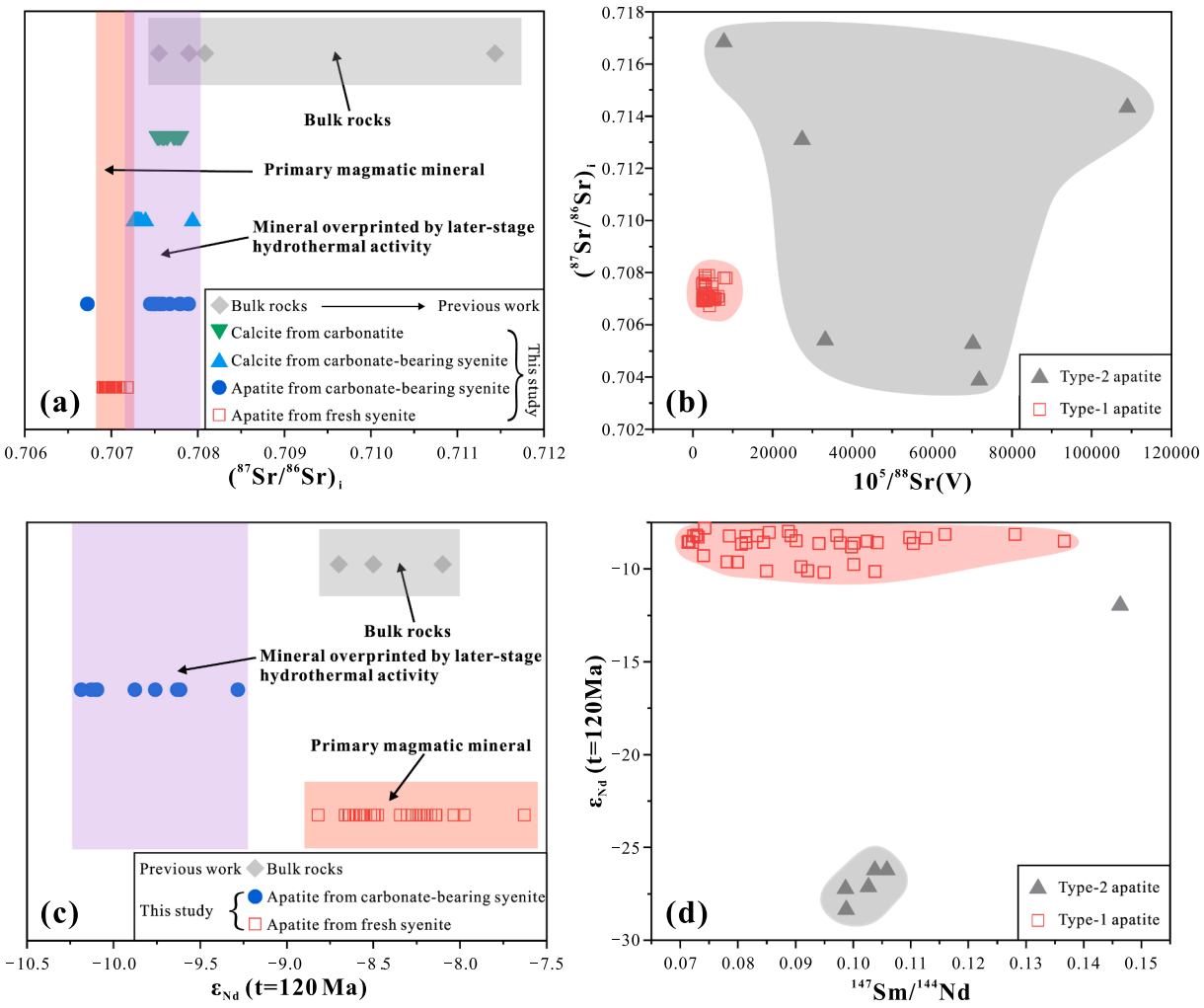


**Fig. 9.** (a) In-situ Sr isotopic composition of apatite and calcite from the Weishan complexes. Previous bulk-rock Sr isotopic data are also shown for comparison (Lan, 2011). Note that bulk rocks have higher and more scattered Sr isotopic ratios than minerals. (b) A plot of $10^5/^{88}Sr$ vs. $(^{87}Sr/^{86}Sr)_{i=120Ma}$ for type-1 and −2 apatite from the Weishan complex. Type-2 apatite has high and much more scattered $(^{87}Sr/^{86}Sr)_{i=120Ma}$ ratios than type-1 apatite. (c) $\varepsilon_{Nd}(t = 120\ Ma)$ values for apatite and calcite from the Weishan complex. Previous bulk-rock Nd isotopic data are also shown for comparison (Lan et al., 2011). (d) A plot of $^{147}Sm/^{144}Nd$ vs. $\varepsilon_{Nd}(t = 120\ Ma)$ for type-1 and −2 apatite from the Weishan complex. Type-2 apatite has obvious lower $\varepsilon_{Nd}(t = 120\ Ma)$ values than type-1 apatite.

$\varepsilon_{Nd}(t)$ values for type-2 apatite is geologically meaningless, as they are xenocrystic in origin.

### 5.4. *In-situ O isotopic composition of zircon*

Zircon grains from syenite sample 21WS03 have a narrow range of $\delta^{18}O_{VSMOW}$(‰) values (5.93 to 6.65 ‰). The average $\delta^{18}O_{VSMOW}$(‰) value is 6.28 ‰ (Appendix Table 4).

## 6. Discussion

### 6.1. *Effective method to obtain the initial Sr-Nd isotopic composition of the Weishan syenite-(carbonatite) complex*

The Sr-Nd isotope compositions of bulk syenite samples have been analyzed before for the Weishan complex (Lan, 2011). The analysis yielded $(^{87}Sr/^{86}Sr)_i$ ratios ranging from 0.707211 to 0.711205, and $\varepsilon_{Nd}(t)$ values from −8.7 to −8.1. It is notable that the newly obtained $\varepsilon_{Nd}(t)$ values (-7.6 to −10.2) from minerals are similar as those of bulk rocks, while the $(^{87}Sr/^{86}Sr)_i$ values (0.70690 to 0.70789) show a much narrower range than those of bulk rocks (Fig. 9a).

The discrepancy between bulk-rock and mineral Sr isotopic data needs to be clarified. Bulk-rocks are characterized by much higher and more variable $^{87}Rb/^{86}Sr$ ratios (0.08–0.40) when compared with apatite and calcite. Hence, the variable initial Sr isotopic ratios of bulk-rocks may be associated with the relatively large uncertainties during subtraction of radiogenic $^{87}Sr$. However, the bulk-rock $(^{87}Sr/^{86}Sr)_i$ values do not have a correlation with the $^{87}Rb/^{86}Sr$ ratios. In addition, the sample with the highest $(^{87}Sr/^{86}Sr)_i$ value maintains a relatively low $^{87}Rb/^{86}Sr$ ratio (0.13) (Lan, 2011). Therefore, the scattered $(^{87}Sr/^{86}Sr)_i$ values of bulk-rock may not be related to inaccurate correction of radiogenic $^{87}Sr$. We note that two types of apatite grains are present in syenite. Type-1 apatite grains show close textural association with magmatic minerals, and display growth zonation in BSE images (Fig. 6a to 6c). They have high REE contents and their $\varepsilon_{Nd}(t)$ values are almost the same as those of bulk syenites. These observations indicate that type-1 apatite grains were crystallized from the REE-rich alkaline magmas. In contrast, type-2 apatite grains are unhedral in shape, and do not display growth zonation in BSE images (Fig. 6d and 6e). They have REE contents much lower than those of type-1 grains. Their $^{87}Sr/^{86}Sr$ ratios are highly scattered and obviously different from those of bulk rocks. Thus, type-2 apatite grains were likely xenocrystic in origin, which were captured during magma ascent (c.f., Lu et al., 2021). We also note that the syenite and carbonatite samples can be variably overprinted by later-stage hydrothermal activity. Although the hydrothermal fluids were initially exsolved from the syenite-(carbonatite) complex, they have more

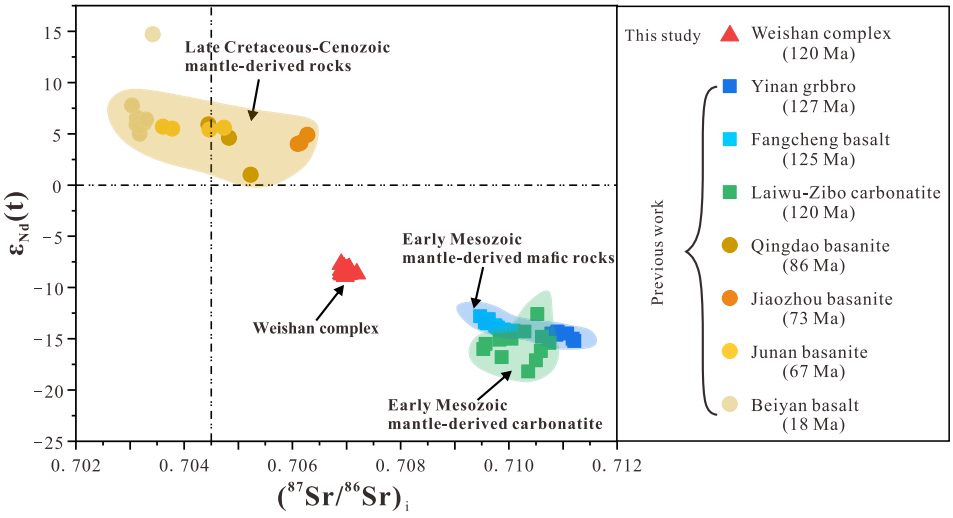


**Fig. 10.** Initial Sr-Nd isotope compositions of Early Mesozoic-Cenozoic mantle-derived magmatic rocks from the Luxi and Jiaodong terranes in NCC, including the Weishan complex (this study); Fangcheng basalt (Zhang et al., 2002; Dai et al., 2019a,b); Yinan gabbro (Xu et al., 2004); Laiwu-Zibo carbonatite (Ying et al., 2004); Beiyan basalt (Xiao et al., 2010); and Junan, Qingdao and Jiaozhou basanite (Dai et al., 2019a,b).

chances to interact with the upper crustal wall-rocks which usually maintain relatively high Sr contents and $^{87}Sr/^{86}Sr$ ratios. Thus, the hydrothermal activity may incorporate a small portion of Sr with more radiogenic Sr isotopic signatures into the syenite-(carbonatite) complex. This hypothesis is supported by the fact that apatite from carbonate-bearing syenite have slightly higher $^{87}Sr/^{86}Sr$ ratios than those from fresh syenite (Fig. 9a).

Given that the syenite-(carbonatite) complex has experienced crustal contamination and hydrothermal alteration, bulk-rock isotopic analysis would yield mixing isotopic signatures. In contrast, in-situ isotopic analyses on primary magmatic minerals tend to reveal the primary isotopic signatures of magmas. This explains why the $(^{87}Sr/^{86}Sr)_i$ ratios of apatite grains have a much narrower range of than those of bulk rocks. Given that the carbonatitic-alkaline melts are particularly rich in REE (including Sm and Nd), the bulk-rock Sm-Nd isotopes are relatively resistant to crustal contamination and hydrothermal alteration. As such, bulk rocks have similar Sm-Nd isotopic compositions as minerals.

According to the above discussion, the initial Sr isotopic ratios and $\varepsilon_{Nd}(t)$ values of the Weishan complex, as represented by apatite from fresh syenite, range from 0.70690 to 0.70719, and from −8.8 to −7.6, respectively. This case indicates that micro-scale isotopic analyses on minerals have advantages to reveal the initial isotopic compositions of primary magmas when bulk rocks experienced open processes. Similar scenarios have been documented in the Phalaborwa carbonatite Complex in South Africa (Wu et al., 2011), the Acasta Gneiss Complex in Canada (Emo et al., 2018), and the Bayan Obo carbonatite in China (Chen et al., 2020).

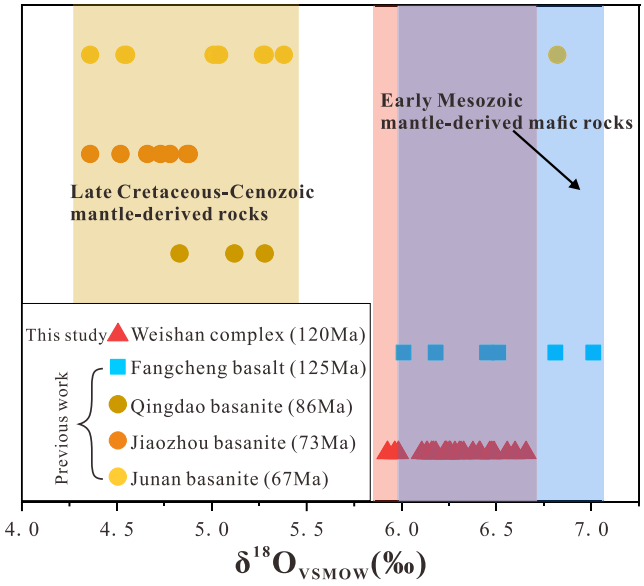


**Fig. 11.** A comparison of the O isotope compositions of the Weishan complex with the Early Mesozoic Fangcheng basalt and Late Mesozoic Junan, Qingdao and Jiaozhou basanite (Dai et al., 2019a,b). The O isotopes of the Weishan complex were obtained from zircon, those for the Fangcheng basalt and Junan, Qingdao and Jiaozhou basanite were obtained from olivine and pyroxene.

### 6.2. *Derivation of the Weishan syenite-(carbonatite) complex through lithosphere-asthenosphere interaction*

A series of Early Mesozoic mantle-derived mafic rocks, such as the Fangcheng basalt and the Yinan gabbro, were generated adjacent to the Weishan complexes in the Luxi terrane (Fig. 2). They are characterized by high $(^{87}Sr/^{86}Sr)_i$ and low $\varepsilon_{Nd}(t)$ values [Fangcheng basalt: $(^{87}Sr/^{86}Sr)_i = 0.70937$ to 0.71010, $\varepsilon_{Nd}(t) = -12.8$ to $-14.2$, Zhang et al., 2002; Daiet al., 2019; Yinan gabbro: $(^{87}Sr/^{86}Sr)_i = 0.71053$ to 0.71121, $\varepsilon_{Nd}(t) = -15.4$ to $-12.6$; Xu et al., 2004]. Moreover, a few mantle-derived carbonatitic intrusions occur in the Laiwu-Zibo area, ~150 km north of the Weishan complex (Fig. 2). The Laiwu-Zibo carbonatites have similar Sr-Nd isotopic compositions as the mafic rocks (0.709526 ± 8 to 0.710607 ± 14 and −18.2 to −14.3, Ying et al., 2004) (Fig. 10). The highly enriched Sr-Nd isotropic signatures indicate that these rocks were derived from an enriched lithospheric mantle with EM-II type affinities. The cause for the isotopic enrichment of the mantle lithosphere is the deep subduction of the Yangtze continental crust beneath the eastern NCC, i.e., partial melting of the subducted lower crust of the Yangtze Craton produced melts (with crustal-like Sr-Nd isotopes) modifying the mantle lithosphere of NCC (Zhang et al., 2002; Guo et al., 2013; Dai et al., 2019a,b).

When compared with the above coeval mantle-derived rocks, the Weishan complex has obviously lower initial Sr isotopic ratios and higher $\varepsilon_{Nd}(t)$ values (Fig. 10), implying that the Weishan complex has a different magma source. Crustal contamination can change the isotopic composition of the primary magmas. However, crustal rocks normally have high Sr isotopic ratios and low $\varepsilon_{Nd}(t)$ values, so crustal contamination is not the cause for the distinctive Sr-Nd isotopic signatures of the Weishan complex. Notably, the late Cretaceous-Cenozoic (86–18 Ma)

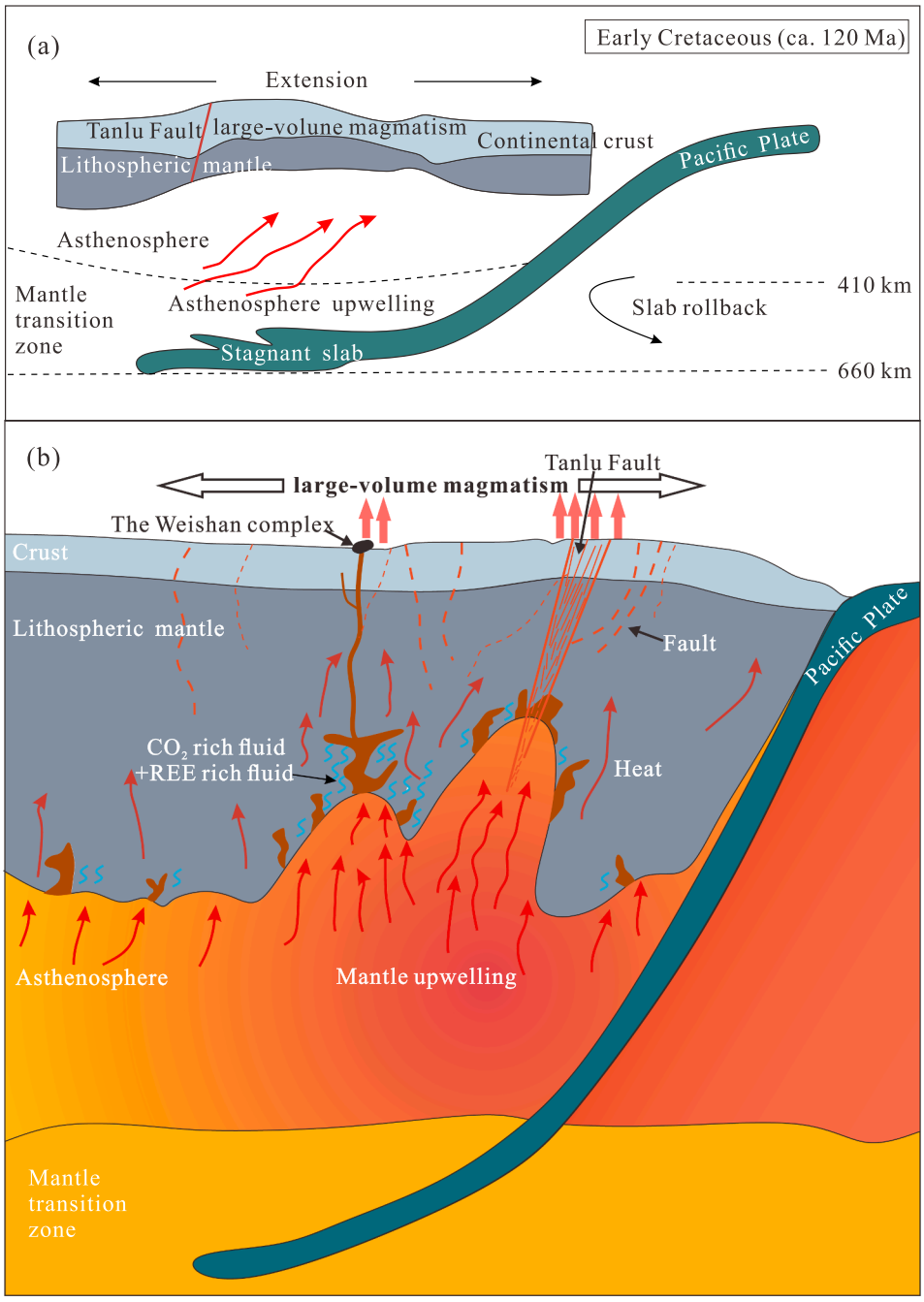


**Fig. 12.** Genetic model (not drawn to scale) for the generation of the Weishan syenite-(carbonatite) complex. (a) Rollback of subducting Paleo-Pacific slab resulted in strong extension and facilitated upwelling of hot, fertile asthenospheric mantle. (b) Ascent of asthenospheric melt tent to occur along *trans*-lithosphere weak zones, such as the Tanlu fault. The reaction of the hot asthenosphere and the overlying enriched lithospheric mantle may result in low degree partial melting of the mantle, forming the Weishan REE-rich carbonatitic-alkaline magmas.

mantle-derived rocks, such as the Beiyan basalt, and Junan, Jiaozhou and Qingdao basanites, have low initial Sr isotopic ratios and high $\varepsilon_{Nd}(t)$ values (Fig. 10). These rocks were thought to be derived from a "younger", fertile lithospheric mantle beneath the eastern NCC (Xiao et al., 2010; Dai et al., 2019a,b). The "younger" lithospheric mantle was generated through Early Mesozoic modification of the "old", refractory lithospheric mantle by asthenosphere-derived components during the destruction of NCC (e.g., Xu et al., 2009; Zheng et al., 2009). The Sr-Nd isotopic compositions of the Weishan complex were just located in the field between those derived from "old" and "young" lithospheric mantle. Therefore, both lithosphere- and asthenosphere-derived components may have been involved in the generation of the Weishan complex.

The zircon oxygen isotopic data lend a further support for this model. We can observe that olivine and pyroxene from the Junan, Jiaozhou and Qingdao basanites that were derived from "younger", fertile lithospheric mantle have lower $\delta^{18}O_{VSMOW}$ values (4.36–6.82 ‰, mostly clustered between 4.36 and 5.38 ‰) (Fig. 11). Zircon grains from the Weishan complex have obviously higher $\delta^{18}O_{VSMOW}$ values than the Junan, Jiaozhou and Qingdao basanites. Such a data distribution pattern may also imply that the Weishan complex was generated through lithosphere-asthenosphere interaction.

### 6.3. *A tectonic model for the generation of the Weishan syenite-(carbonatite) complex*

The Weishan complex was generated in the Early Mesozoic, at the climax timing of destruction of NCC. As such, its formation is logically related to this tectonic event. The geodynamic drive the destruction of NCC has been extensively studied (e.g., Wu et al., 2005; Zhai et al., 2007; Zheng et al., 2009; Zhu et al., 2012; Zhu et al., 2019). Since late

Paleozoic, the NCC has been affected by plate subduction and collision from different directions, including southward subduction of Paleo-Asian oceanic plate, northward subduction and collision of the Yangtze Block, and westward subduction of Paleo-Pacific Plate. All these tectonic activities will affect on the dynamic, thermal and chemical states of the NCC. Subduction of the Paleo-Pacific plate, in particular, may have the prominent effect on the destruction of NCC, because subduction and dehydration of the oceanic plate can release significant amounts of water into the overriding lithospheric mantle and, as a consequence, the viscosity of the lithosphere is significantly lowered and the continental lithosphere can be severely weakened (Zhu et al., 2019). Integration of available data suggests that the subduction of the western Pacific plate was initiated as early as Early Jurassic (Xu et al., 2013; Wang et al., 2015). There has been a rollback of subducting Paleo-Pacific slab and the retreatment of subduction zones since the Early Cretaceous (Zhu et al., 2015, 2021). This resulted in strong extension and formed a widely spread pull apart basins and metamorphic core complexes in the eastern NCC. The space left by lithospheric thinning will facilitate upwelling of hot, fertile asthenospheric mantle that was cooled and formed the juvenile lithospheric mantle (Fig. 12a). We note the Weishan complex is located adjacent to the Tan-Lu fault, which is a *trans*-lithosphere weak zone in the region. Such a weak zone is expected to facilitate the ascent and migration of asthenospheric melt and enhanced lithosphere-asthenosphere reaction. The reaction of the hot asthenospheric magma and the overlying enriched lithospheric mantle may result in low degree partial melting of the mantle, forming the Weishan REE-rich carbonatitic-alkaline magmas (Fig. 12b). The extensional setting would further facilitate ascent and emplacement of ore-fertile magmas.

### 6.4. Implication for the generation of REE-rich carbonatite-alkaline complex

More than 60% REE resources around the world come from carbonatite-alkaline systems (Weng et al., 2015). However, it is still not well understood why a small number of carbonatite-alkaline occurrences are more prone to REE mineralization relative to other majorities. Several Early Cretaceous carbonatite (-alkaline) intrusions, including the Weishan complex and the Laiwu-Zibo carbonatitic dykes or sills, can be found in the eastern NCC. The former contains the third largest REE deposit in China, while the latter ones do not show REE enrichments. Such a contrast provides an opportunity to explore factors facilitating REE mineralization. We distinguish the Weishan complex from the other intrusions by the presence of asthenosphere-derived components in its magma source. Thus, magma source may be an important factor influencing the fertility of carbonatitic(-alkaline) melts. It has been proposed that asthenosphere can be locally enriched in metals (e.g., REE and Nb) and volatiles (Wu et al., 2013; Chandra et al., 2018), which may be associated with deep subduction and recycling of crustal materials (Cheng et al., 2017; Banerjee and Chakrabarti, 2019). It is evidenced by certain REE and/or Nb-rich carbonatites that were mainly derived from the asthenosphere, such as the Oka carbonatite in Canada (Chen et al., 2013, 2015) and the Bear Lodge carbonatite in America (Moore et al., 2015). Both volatiles and REE are low-solidus components, and thus they can be concentrated in low-degree partial melts during asthenosphere uprising and metasomatized a part of the mantle lithosphere. Further melting of the metasomatized lithospheric mantle may produce the REE-rich carbonatite. Such a genetic model has been proposed for the Ambar Dongar REE deposit in India (Chandra et al., 2018) and a series of REE deposits in the Kola Penisula in Russia (Zaitsev et al., 2014). Similarly, asthenosphere uprising and melting may also play a significant role for the REE mineralization in the Weishan complex. This speculation is subject to further research.

## 7. Conclusions

In-situ Sr, Nd and O isotopic studies of apatite, calcite and zircon from the Mesozoic Weishan REE-rich syenite-(carbonatite) complex, Northern China, help to understand the nature of the magma source of the complex and provide insights into the factors facilitating REE mineralization. The main conclusions of this study include:

(1) In-situ isotopic analyses of minerals can be more reliable to determine the nature of primary magmas than bulk-rock analyses.

(2) The primary magma of the Weishan complex had initial Sr isotopic ratios ranging from 0.70690 to 0.70719, and $\varepsilon_{Nd}(t)$ values from −8.8 to −7.6. Such results indicate that both lithospheric and asthenospheric mantle have contributed to the generation of the complex.

(3) Generation of the Weishan complex was related to the upwelling of the asthenosphere induced by the rollback of subducting Paleo-Pacific slab.

(4) Involvement of asthenosphere-derived components may play an important role in the enrichment of REE in the Weishan complex.

## CRediT authorship contribution statement

**Xi Zeng:** Data curation, Writing – original draft. **Xiaochun Li:** Funding acquisition, Supervision, Writing – review & editing. **Hongrui Fan:** Investigation. **Tingguang Lan:** Investigation, Writing – review & editing. **Jun Lan:** Investigation. **Jianhui Su:** Writing – review & editing. **Peng Zhang:** Investigation. **Kuifeng Yang:** Investigation. **Xinfu Zhao:** Writing – review & editing.

## Declaration of Competing Interest

The authors declare that they have no known competing financial interests or personal relationships that could have appeared to influence the work reported in this paper.

## Acknowledgement

We are most grateful to the staff of the Nanjing FocuMS Analysis Lab, the Wuhan Sample Solution Analytical Technology Co., Ltd and the Institute of Geology and Geophysics (IGG) for help in obtaining the data. Constructive discussions with Haidong She, Zhenyu Wang, Langye Zhao, Zhengjie Qiu, Shuangliang Liu and Hongtao Li have substantially improved the manuscript. Prof. Mei-Fu Zhou and anonymous reviewers are greatly appreciated for their constructive reviews. This study was financially supported by research grants from National Natural Science Foundation of China (No. 42072092, 41930430).

## Appendix A. Supplementary data

Supplementary data to this article can be found online at https://doi.org/10.1016/j.jseaes.2022.105191.

## References

Banerjee, A., Chakrabarti, R., 2019. A geochemical and Nd, Sr and stable Ca isotopic study of carbonatites and associated silicate rocks from the ~65 Ma old Amba dongar carbonatite complex and the Phenai Mata igneous complex, Gujarat, India: Implications for crustal contamination, carbonate recycling, hydrothermal alteration and source-mantle mineralogy. Lithos 326, 572–585.

Bell, K. 2020. Carbonatites. In Elias S. and Alderton D. eds. Encyclopedia of Geology, 2nd edition.

Bell, K., Simonetti, A., 2010. Source of parental melts to carbonatites–critical isotopic constraints. Mineralogy and Petrology 98 (1), 77–89.

Chandra, J., Paul, D., Viladkar, S.G., Sensarma, S., 2018. Origin of the Amba Dongar carbonatite complex, India and its possible linkage with the Deccan Large Igneous Province. Geological Society, London, Special Publications 463 (1), 137–169.

Chen, W., Kamenetsky, V.S., Simonetti, A., 2013. Evidence for the alkaline nature of parental carbonatite melts at Oka complex in Canada. Nature Communications 4 (1), 1–6.

Chen, W., Liu, H.-Y., Lu, J., Jiang, S.-Y., Simonetti, A., Xu, C., Zhang, W., 2020. The formation of the ore-bearing dolomite marble from the giant Bayan Obo REE-Nb-Fe deposit, Inner Mongolia: insights from micron-scale geochemical data. Mineralium Deposita 55 (1), 131–146.

Chen, W., Simonetti, A., 2015. Isotopic (Pb, Sr, Nd, C, O) evidence for plume-related sampling of an ancient, depleted mantle reservoir. Lithos 216, 81–92.

Cheng, Z.G., Zhang, Z.C., Hou, T., Santosh, M., Chen, L.L., Ke, S., Xu, L.J., 2017. Decoupling of Mg–C and Sr–Nd–O isotopes traces the role of recycled carbon in magnesiocarbonatites from the Tarim Large Igneous Province. Geochimica et Cosmochimica Acta 202, 159–178.
Dai, F.-Q., Zhao, Z.-F., Zheng, Y.-F., Sun, G.-C., 2019a. The geochemical nature of mantle sources for two types of Cretaceous basaltic rocks from Luxi and Jiaodong in east-central China. Lithos 344-345, 409–424.
Dai, H.K., Zheng, J.P., Xiong, Q., Su, Y.P., Pan, S.K., Ping, X.Q., Zhou, X. 2019. Fertile lithospheric mantle underlying ancient continental crust beneath the northwestern North China craton: Significant effect from the southward subduction of the Paleo–Asian Ocean. Bulletin 131(1-2), 3-20.
Davis, G.A., Zheng, Y.D., Wang, C., Darby, B.J., Zhang, C.H., Gehrels, G., 2001. Mesozoic tectonic evolution of the Yanshan fold and thrust belt, with emphasis on Hebei and Liaoning Provinces northern China. Geological Society of America Memoirs 194, 171–198.
Deines, P., 1989. Stable isotope variations in carbonatites. Carbonatites 301–357.
Duan, Z., Li, J.-W., 2017. Zircon and titanite U-Pb dating of the Zhangjiawa iron skarn deposit, Luxi district, North China Craton: Implications for a craton-wide iron skarn mineralization. Ore Geology Reviews 89, 309–323.
Eiler, J.M., Farley, K.A., Valley, J.W., Hauri, E., Craig, H., Hart, S.R., Stolper, E.M., 1997. Oxygen isotope variations in ocean island basalt phenocrysts. Geochimica et Cosmochimica Acta 61 (11), 2281–2293.
Emo, R.B., Smit, M.A., Schmitt, M., Kooijman, E., Scherer, E.E., Sprung, P., Bleeker, W., Mezger, K., 2018. Evidence for evolved Hadean crust from Sr isotopes in apatite within Eoarchean zircon from the Acasta Gneiss Complex. Geochimica et Cosmochimica Acta 235, 450–462.
Fan, H.R., Hu, F.F., Yang, J.H., Shen, K., Zhai, M.G., 2005. Fluid evolution and large-scale gold metallogeny during Mesozoic tectonic transition in the eastern Shandong province. Acta Petrologica Sinica 21, 1317–1328 in Chinese with English abstract.
Griffin, W.L., Andi, Z., O'reilly, S.Y., Ryan, C.G., 1998. Phanerozoic evolution of the lithosphere beneath the Sino-Korean craton. Mantle dynamics and plate interactions in East Asia 27, 107–126.
Guo, P., Santosh, M., Li, S.R., 2013. Geodynamics of gold metallogeny in the Shandong Province, NE China: an integrated geological, geophysical and geochemical perspective. Gondwana Research 24 (3–4), 1172–1202.
Hoernle, K., Tilton, G., Le Bas, M.J., Duggen, S., Garbe-Schönberg, D., 2002. Geochemistry of oceanic carbonatites compared with continental carbonatites: mantle recycling of oceanic crustal carbonate. Contributions to Mineralogy and Petrology 142 (5), 520–542.
Hofmann, A.W., Hargraves, R.B., 2014. Diffusion in natural silicate melts: a critical review. Physics of magmatic processes 385–418.
Hou, Z.Q., Liu, Y., Tian, S.H., Yang, Z.M., Xie, Y.L., 2015. Formation of carbonatite-related giant rare-earth-element deposits by the recycling of marine sediments. Scientific Reports 5 (1), 10231.
Hu, F.F., Wang, Y., Fan, H.R., Zheng, X.L., Jiao, P., 2010. Geochronology and ore-forming fluids in the Jinchang skarn gold-copper deposit, Yinan County, western Shandong Province. Acta Petrologica Sinica 26 (5), 1503–1511 in Chinese with English abstract.
Jia, Y.H., Liu, Y., 2020. REE Enrichment during Magmatic-Hydrothermal Processes in Carbonatite-Related REE Deposits: A Case Study of the Weishan REE Deposit. China. Minerals 10 (1), 25.
Jones, A.P., Genge, M., Carmody, L., 2013. Carbonate melts and carbonatites. Reviews in Mineralogy and Geochemistry 75 (1), 289–322.
Lan, T.G., 2011. Mesozoic alkaline rocks and related deposits from the southeastern North China Craton. Ph.D Thesis, Chinese Academy of Sciences.
Lan, T.G., Fan, H.R., Hu, F.F., Yang, K.F., Wang, Y., 2011. Genesis of the Weishan REE deposit, Shandong Province: evidences from Rb-Sr isochron age, LA-MC-ICPMS Nd isotopic compositions and fluid inclusions. Geochimica 40, 428–442.
Lan, T.-G., Fan, H.-R., Santosh, M., Hu, F.-F., Yang, K.-F., Yang, Y.-H., Liu, Y., 2012. Early Jurassic high-K calc-alkaline and shoshonitic rocks from the Tongshi intrusive complex, eastern North China Craton: implication for crust–mantle interaction and post-collisional magmatism. Lithos 140-141, 183–199.
Le Maitre, R.W., 2002. Igneous Rocks: A Classification and Glossary of Terms. Cambridge University Press, Cambridge, U.K., p. 236
Lee, W.J., Wyllie, P.J., 1998. Processes of crustal carbonatite formation by liquid immiscibility and differentiation, elucidated by model systems. Journal of Petrology 39 (11–12), 2005–2013.
Li, S.G., Xiao, Y.L., Liou, D.L., Chen, Y.Z., Ge, N.J., Zhang, Z.Q., Shen, S.S., Cong, B.L., Zhang, R.Y., Hart, S.R., Wang, S.S., 1993. Collision of the North China and Yangtse Blocks and formation of coesite-bearing eclogites: timing and processes. Chemical Geology 109 (1–4), 89–111.
Li, X.H., Tang, G.Q., Gong, B., Yang, Y.H., Hou, K.J., Hu, Z.C., Li, Q.L., Liu, Y., Li, W.X., 2013. Qinghu zircon: A working reference for microbeam analysis of U-Pb age and Hf and O isotopes. Chinese Science Bulletin 58 (36), 4647–4654.
Liu, C.Z., Wu, F.Y., Chung, S.L., Li, Q.L., Sun, W.D., Ji, W.Q., 2014. A 'hidden' $^{18}$O-enriched reservoir in the sub-arc mantle. Scientific reports 4 (1), 1–6.
Lu, J., Chen, W., Ying, Y., Jiang, S., Zhao, K., 2021. Apatite texture and trace element chemistry of carbonatite-related REE deposits in China: Implications for petrogenesis. Lithos 398-399, 106276. https://doi.org/10.1016/j.lithos.2021.106276.
Manthilake, M.A.G.M., Sawada, Y., Sakai, S., 2008. Genesis and evolution of Eppawala carbonatites, Sri Lanka. Journal of Asian earth sciences 32 (1), 66–75.
Meng, Q.R., Zhang, G.W., 1999. Timing of collision of the North and South China blocks: controversy and reconciliation. Geology 27 (2), 123–126.
Menzies, M.A., Fan, W.M., Zhang, M., 1993. Palaeozoic and Cenozoic lithoprobes and the loss of >120 km of Archaean lithosphere, Sino-Korean craton, China. Geological Society, London, Special Publications 76 (1), 71–81.
Mitchell, R.H., 2005. Carbonatites and carbonatites and carbonatites. The Canadian Mineralogist 43 (6), 2049–2068.
Moore, M., Chakhmouradian, A.R., Mariano, A.N., Sidhu, R., 2015. Evolution of rare-earth mineralization in the Bear Lodge carbonatite, Wyoming: Mineralogical and isotopic evidence. Ore Geology Reviews 64, 499–521.
Nguyen Thi, T., Wada, H., Ishikawa, T., Shimano, T., 2014. Geochemistry and petrogenesis of carbonatites from South Nam Xe, Lai Chau area, northwest Vietnam. Mineralogy and Petrology 108 (3), 371–390.
Simandl, G.J., Paradis, S., 2018. Carbonatites: related ore deposits, resources, footprint, and exploration methods. Applied Earth Science 127 (4), 123–152.
Simonetti, A., Goldstein, S.L., Schmidberger, S.S., Viladkar, S.G., 1998. Geochemical and Nd, Pb, and Sr isotope data from Deccan alkaline complexes—inferences for mantle sources and plume–lithosphere interaction. Journal of Petrology 39 (11–12), 1847–1864.
Verplanck, P.L., Mariano, A.N., Mariano Jr, A. 2016. Rare earth element ore geology of carbonatites.
Wang, C., Liu, J.C., Zhang, H.D., Zhang, X.Z., Zhang, D.M., Xi, Z.X., Wang, Z.J., 2019. Geochronology and mineralogy of the Weishan carbonatite in Shandong province, eastern China. Geoscience Frontiers 10 (2), 769–785.
Wang, F., Xu, W.-L., Xu, Y.-G., Gao, F.-H., Ge, W.-C., 2015. Late Triassic bimodal igneous rocks in eastern Heilongjiang Province, NE China: Implications for the initiation of subduction of the Paleo-Pacific Plate beneath Eurasia. J Asian Earth Sci 97, 406–423.
Wang, S.J., Wan, Y.S., Zhang, C.J., Yang, E.X., Song, Z.Y., Wang, L.F., Zhang, F.Z., 2008. Major advanced development gained in studying early cambrian geology in luxi area. Land and Resources in Shandong Province (in Chinese with English abstract).
Weng, Z.H., Jowitt, S.M., Mudd, G.M., Haque, N., 2015. A detailed assessment of global rare earth element resources: opportunities and challenges. Economic Geology 110 (8), 1925–1952.
Wiedenbeck, M., Hanchar, J.M., Peck, W.H., Sylvester, P., Valley, J., Whitehouse, M., Kronz, A., Morishita, Y., Nasdala, L., Fiebig, J., Franchi, I., Girard, J.P., Greenwood, R.C., Hinton, R., Kita, N., Mason, P.R.D., Norman, M., Ogasawara, M., Piccoli, P.M., Rhede, D., Satoh, H., Schulz-Dobrick, B., Skar, O., Spicuzza, M.J., Terada, K., Tindle, A., Togashi, S., Vennemann, T., Xie, Q., Zheng, Y.F., 2004. Further characterisation of the 91500 zircon crystal. Geostandards and Geoanalytical Research 28 (1), 9–39.
Woolley, A.R., Bailey, D.K., 2012. The crucial role of lithospheric structure in the generation and release of carbonatites: geological evidence. Mineralogical Magazine 76 (2), 259–270.
Woolley, A.R., Kjarsgaard, B.A., 2008. Paragenetic types of carbonatite as indicated by the diversity and relative abundances of associated silicate rocks: evidence from a global database. The Canadian Mineralogist 46 (4), 741–752.
Wu, F.Y., Arzamastsev, A.A., Mitchell, R.H., Li, Q.L., Sun, J., Yang, Y.H., Wang, R.C., 2013. Emplacement age and Sr–Nd isotopic compositions of the Afrikanda alkaline ultramafic complex. Kola Peninsula, Russia: Chemical Geology 353, 210–229.
Wu, F.Y., Lin, J.Q., Wilde, S.A., Yang, J.H., 2005. Nature and significance of the Early Cretaceous giant igneous event in eastern China. Earth and Planetary Science Letters 233 (1–2), 103–119.
Wu, F.-Y., Yang, Y.-H., Li, Q.-L., Mitchell, R.H., Dawson, J.B., Brandl, G., Yuhara, M., 2011. In situ determination of U-Pb ages and Sr–Nd–Hf isotopic constraints on the petrogenesis of the Phalaborwa carbonatite Complex. South Africa. Lithos 127 (1-2), 309–322.
Xiao, W., Windley, B.F., Hao, J., Zhai, M., 2003. Accretion leading to collision and the Permian Solonker suture, Inner Mongolia, China: Termination of the central Asian orogenic belt. Tectonics 22 (6), n/a–n/a.
Xiao, Y., Zhang, H.-F., Fan, W.-M., Ying, J.-F., Zhang, J., Zhao, X.-M., Su, B.-X., 2010. Evolution of lithospheric mantle beneath the Tan-Lu fault zone, eastern North China Craton: evidence from petrology and geochemistry of peridotite xenoliths. Lithos 117 (1-4), 229–246.
Xu, W.L., Yang, D.B., Pei, F.P., Wang, F., Wang, W., 2009. Mesozoic lithospheric mantle modified by delaminated lower continental crust in the North China Craton: constraints from compositions of amphiboles from peridotite xenoliths. Journal of Jilin University (Earth Science Edition) 39 (4), 606–617.
Xu, W.L., Pei, F.P., Wang, F., Meng, E., Ji, W.Q., Yang, D.B., Wang, W., 2013. Spatial–temporal relationships of Mesozoic volcanic rocks in NE China: constraints on tectonic overprinting and transformations between multiple tectonic regimes. Journal of Asian Earth Sciences 74, 167–193.
Xu, Y.G., Ma, J.L., Huang, X.L., Iizuka, Y., Chung, S.L., Wang, Y.B., Wu, X.Y., 2004. Early Cretaceous gabbroic complex from Yinan, Shandong Province: petrogenesis and mantle domains beneath the North China Craton. International Journal of Earth Sciences 93 (6), 1025–1041.
Yang, Z., Zhang, X., Yuan, L., 2021. Tracking decratonization process along a cratonic edge through late Permian to late Triassic magmatic flare-up in northwestern Liaoning. North China Craton. Lithos 380-381, 105916. https://doi.org/10.1016/j.lithos.2020.105916.
Yaxley, G.M., Anenburg, M., Tappe, S., Decree, S., Guzmics, T., 2022. Carbonatites: Classification, Sources, Evolution, and Emplacement. Annu. Rev. Earth Planet. Sci. 50 (1) https://doi.org/10.1146/earth.2022.50.issue-110.1146/annurev-earth-032320-104243.
Yaxley, G.M., Brey, G.P., 2003. Petrological constraints on carbonated eclogite as a source of carbonatites. Geochimica et Cosmochimica Acta Supplement 67 (18), 561.
Ying, J.F., Zhou, X.H., Zhang, H.F., 2004. Geochemical and isotopic investigation of the Laiwu-Zibo carbonatites from western Shandong Province, China, and implications for their petrogenesis and enriched mantle source. Lithos 75 (3–4), 413–426.

Zaitsev, A.N., Wall, F., Chakhmouradian, A.R. 2014. Rare-earth elements minerals in carbonites of the Kola Alkaline province (northern Fennoscandia). In 1st European Rare Earth Resources Conference (Milos, 07.09. 2014).–Greece (pp. 343-347).

Zhai, M., Fan, Q., Zhang, H., Sui, J., Shao, Ji'an, 2007. Lower crustal processes leading to Mesozoic lithospheric thinning beneath eastern North China: underplating, replacement and delamination. Lithos 96 (1-2), 36–54.

Zhang, H.F., Sun, M., Zhou, X.H., Fan, W.M., Zhai, M.G., Yin, J.F., 2002. Mesozoic lithosphere destruction beneath the North China Craton: evidence from major-, trace-element and Sr–Nd–Pb isotope studies of Fangcheng basalts. Contributions to Mineralogy and Petrology 144 (2), 241–254.

Zhao, G.C., Wilde, S.A., Cawood, P.A., Lu, L.Z., 1998. Thermal evolution of Archean basement rocks from the eastern part of the North China Craton and its bearing on tectonic setting. International Geology Review 40 (8), 706–721.

Zhao, G.C., Wilde, S.A., Cawood, P.A., Sun, M., 2001. Archean blocks and their boundaries in the North China Craton: lithological, geochemical, structural and P-T path constraints and tectonic evolution. Precambrian Research 107 (1–2), 45–73.

Zheng, J.P., 2009. Comparison of mantle-derived matierals from different spatiotemporal settings: Implications for destructive and accretional processes of the North China Craton. Chinese Science Bulletin 54 (19), 3397–3416.

Zhou, W.W., Cai, J.H., Yan, G.H., 2013. The geochemical characteristics and geological significance of alkaline complex in Chishan of Shandong province. North-western Geology 46 (4), 93–105 in Chinese with English abstract.

Zhu, G., Liu, C., Gu, C.C., Zhang, S., Li, Y.J., Su, N., Xiao, S.Y., 2018. Oceanic plate subduction history in the western Pacific Ocean: Constraint from late Mesozoic evolution of the Tan-Lu Fault Zone. Science China Earth Sciences 61 (4), 386–405.

Zhu, G., Wang, W., Gu, C.C., Zhang, S., Liu, C., 2016. Late Mesozoic evolution history of the Tan-Lu Fault Zone and its indication to destruction processes of the North China Craton. Acta Petrologica Sinica 32 (4), 935–949 in Chinese with English abstract.

Zhu, R.X., Fan, H.R., Li, J.W., Meng, Q.R., Li, S.R., Zeng, Q.D., 2015. Decratonic gold deposits. Science China Earth Sciences 58 (9), 1523–1537.

Zhu, R., Sun, W., 2021. The big mantle wedge and decratonic gold deposits. Science China Earth Sciences 64 (9), 1451–1462.

Zhu, R.X., Xu, Y.G., 2019. The subduction of the west Pacific plate and the destruction of the North China Craton. Science China Earth Sciences 62 (9), 1340–1350.

Zhu, R.X., Yang, J.H., Wu, F.Y., 2012. Timing of destruction of the North China Craton. Lithos 149, 51–60.

Zhu, Y.S., Yang, J.H., Sun, J.F., Wang, H., 2017. Zircon Hf-O isotope evidence for recycled oceanic and continental crust in the sources of alkaline rocks. Geology 45 (5), 407–410.